Artemisinin-Acetylenedicarboxylic Acid Cocrystal: Screening, Structure determination, and Physicochemical Property Characterisation

Jay Makadia[a], Shadrack J. Madu[a], Randolph Arroo[a], Colin C. Seaton[b], Mingzhong Li[a*]

[a]School of Pharmacy, De Montfort University, Leicester, LE1 9BH, UK
[b]Faculty of Life Sciences, School of Chemistry and Bioscience, University of Bradford, Bradford, BD7 1DP, UK

Abstract

Artemisinin is used to treat multi-drug resistant strains of malaria and is also in the early stages of development as an anti-cancer drug. However, the usage of artemisinin is limited due to a low aqueous solubility. Herein a large scale of cocrystal screening of artemisinin was conducted using both computational and experimental approaches, leading to a new 2:1 artemisinin and acetylenedicarboxylic acid (ART^2-ACA) cocrystal. ART^2-ACA crystallises in the P $2_12_12_1$ space group of orthorhombic system with the cell parameters a = 10.5089 Å, b = 24.083 Å, c = 6.4952 Å. The asymmetric unit of the cocrystal contains one ART molecules and a half of ACA molecule, assembled into discrete trimeric units held together by two supramolecular heterosynthons. It was shown that ART^2-ACA cocrystals are of higher solubility and faster dissolution rate compared to the parent drug of artemisinin.

Key words: artemisinin, cocrystal, Malaria, dissolution performance parameter.

* Corresponding Author: Email: mli@dmu.ac.uk; Tel: +44(0)116 257 7132.

Introduction

Artemisinin (ART) is one of important antimalarial compounds isolated from Chinese medical herb Qian Hao (artemisia annua) and it is a superior plasmocidal and blood schizontocidal agent compared to conventional antimalarial drugs, such as chloroquine and quinine, without obvious adverse effects in patients[1, 2]. However, artemisinin has low aqueous solubility, resulting in poor and erratic absorption upon oral administration, typically 8-10% of bioavailability[3-6]. In order to overcome the problems, current work is focused on development of semisynthetic derivatives of artemisinin, such as arteether, artemether, artesunate, artelinate and dihydroartemisinin, to achieve desired physicochemical properties for oral formulations[1, 2]. Despite being effective, these derivatives are limited in the treatment of malaria by its high cost, short half-life, toxicity and drug resistance[7, 8]. Therefore, it is urgently needed to find new solid forms of artemisinin with required properties, in particular solubility and dissolution rate, within oral dosage forms to increase its bioavailability and effective.

Over the last decade, pharmaceutical cocrystals have drawn significant interests for its ability to enhance solubility and dissolution rate of poorly water-soluble pharmaceutical active ingredients (APIs), through supramolecular interactions between the API and a coformer[9, 10]. Cocrystals of APIs are particularly attractive to modify the solid state properties of the parent API crystals when salt formation is infeasible or when existing salts fail to exhibit suitable properties, such as weakly ionizable or non-ionizable molecules[11]. The structure of artemisinin is shown in Fig. 1 (a), which is a sesquiterpene lactone containing an unusual peroxide bridge and it exists as two polymorphs or crystalline forms, i.e., orthorhombic and triclinic polymorphs[12]. Although the solubility of the triclinic form of ART is higher than its orthorhombic form, it is still well below the requirement for development of an oral dosage form formulation[12, 13]. Due to its lack of ionisable sites, there is no salt form of artemisinin reported in the literature. Two cocrystal forms of artemisinin were reported in the literature, i.e., 1:1 cocrystal with orcinol (ART-ORC) and 2:1 cocrystal with resorcinol (ART^2-RES) through a large scale cocrystal screening involving 75 potential coformers[14]. Recently *in vitro* and *in vivo* studies have demonstrated that both of artemisinin cocrystals can significantly enhance its clinical performance in comparison with the parent drug of artemisinin, suggesting the potential benefit of an artemisinin cocrystal formulation as a promising drug delivery model for bioavailability enhancement for antimalarial therapy[6, 15]. Unfortunately, the oral toxicity of the coformers of orcinol and resorcinol is a matter of concern if these cocrystals are developed into commercial products for human use[16, 17].

The motivation of the work was to discover novel artemisinin cocrystals potentially for human use. In this work, pre-screening was carried out using tools of both a molecular complementarity screening[18, 19] and virtual screening based on molecular electrostatic potential surfaces[20-22]. The experimental screening was conducted by co-grinding a 1:1 stoichiometric ratio mixture of artemisinin and a coformer which was on the top 20 in the ranking list determined by the pre-screening tools with or without a drop of a solvent for 30 mins. Four different polarity solvents were used in a liquid-assisted grinding experiment, including acetone, ethanol, methanol, and ethyl acetate. The samples were analysed by powder x-ray diffraction (PXRD), fourier transform infrared spectroscopy (FTIR), and thermal analysis [i.e., differential scanning calorimeter (DSC) and hot stage microscopy (HSM)] for confirmation of cocrystal formation. A new cocrystal was discovered as 2:1 artemisinin-acetylenedicarboylic acid (ART^2-ACA). Solution evaporation experiments were subsequently undertaken to obtain single cocrystals of ART^2-ACA suitable for structure determination using a single crystal XRD analysis. The pharmaceutical relevant properties, i.e., solubility and dissolution rate of the newly discovered ART^2-ACA cocrystals, have been evaluated. It has been shown that ART^2-ACA can increase the solubility of artemisinin with a fast dissolution rate. Acetylenedicarboxylic acid [ACA shown in Fig. 1(b)] is a dicarboxylic acid containing a carbon-carbon triple bond, which is used as a common precursor in organic synthesis and serves as a pharmaceutical intermediate. Although ACA is of acute oral toxicity[23], it could have potential for clinical use, for example, ACA can form cocrystals with meloxicam used in the treatment of rheumatoid arthritis[24].

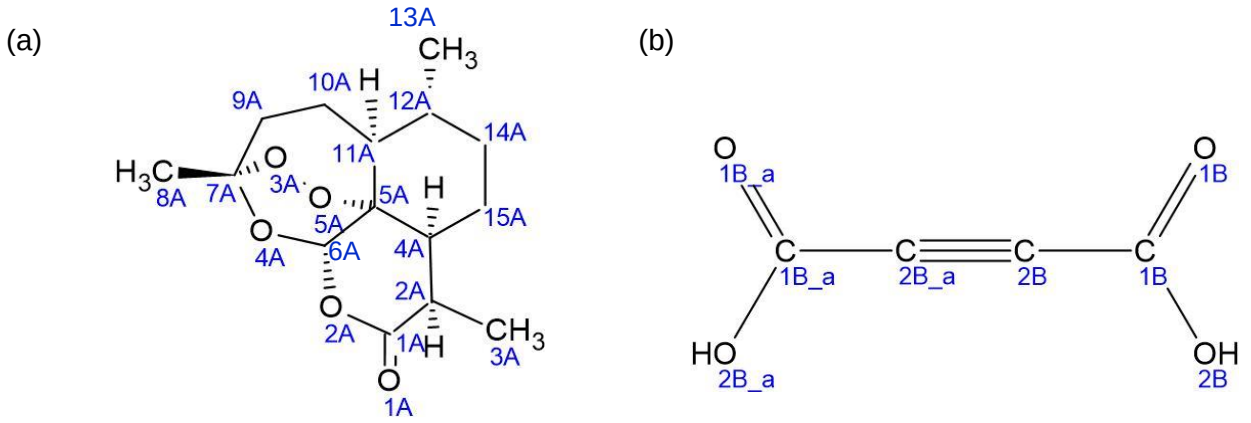

Fig. 1. Chemical structures of (a) Artemisinin and (b) Acetylenedicarboxylic

Materials and Methods

Materials

Artemisinin (ART, ≥98% purity), furosemide (FUR, ≥98% purity), niflumic acid (NFA, ≥98% purity), hydrochlorothiazide (HCT, ≥95% purity), quercetin (QUC, ≥95% purity), flufenamic acid (FFA, ≥97% purity), 4-hydroxybenzohydrazide (HBD, ≥97% purity), Oxalic acid (OXA, ≥99% purity) were purchased from Sigma-Aldrich (Dorset, UK). Etidronic acid (HEDP, ≥96% purity), riboflavin (RFN, ≥98% purity), acedoben (ADB, ≥98% purity), 4-hydroxybenzoic acid (HBA, ≥99% purity), Pamoic acid (PMA, ≥99% purity), 4-aminobenzoic acid (ABA, ≥99% purity), 2-amino-5-methylbenzoic acid (AMBA, ≥97% purity), Hesperetin (HES, ≥97% purity), Phthalamide (PTA, ≥97% purity) were purchased from Alfa Aesar (Lancaster, UK). Biotin (BIO, ≥98% purity), acetylenedicarboxylic acid (ACA, ≥98% purity), amodiaquine dihydrochloride dihydrate (AQD, ≥99% purity) were purchased from Arcos Organics (Geel, Belgium). Resveratrol (Trans) (RSV, ≥98% purity) was purchased from Cayman Chemicals (Michigan, USA). HPLC grade of methanol (MeOH), ethanol (EtOH), or acetonitrile (ACN) and analytical grade of acetone (ACE), ethyl acetate (EtAC), or chloroform (CF) were purchased from Fisher Scientific (Loughborough, UK) used in for all experiments. Double distilled water (DDW) was generated from a Bi-Distiller (WSC044.MH3.7, Fistreem International Limited, Loughborough, UK) in house and used throughout the study.

Methods

Ab initio screening

An initial cocrystal screening was undertaken by the Cambridge Structure Database (CSD) search (ConQuest v2020.2.0) using the keywords of artemisinin and its molecular structure. A molecular complementarity screening tool which results in a simple pass or fail filtering methodology for the formation of cocrystals between ART and a chosen coformer (in total 80 coformers selected) was evaluated by the CSD Molecular Complementarity tools (Mercury v2020.2.0)[18, 19].

For the virtual screening tool, the selected coformers and ART were drawn and then their energies were minimized using DFT B3LYP/6-31+G* ab initio calculations. The local maxima and minima sites on the MEPS (mapped on electron density isosurface with isovalue of 0.002 Bohr $Å^{-3}$) of each molecule were identified using Spartan 18 (v1.4.5). Local maxima and minima values were converted into corresponding hydrogen bond donor and acceptor interaction site parameters (α and β). The detailed parameters used in calculations of energy difference and probability were described by Hunter and coworkers[20] and the values of each pair at 1:1 molar ratio were given in Table S3 in the supporting materials.

Cocrystal screening via neat grinding (NG) and liquid-assisted grinding (LAG)

In the screening experiments, a total of 200 mg of ART with a selected coformer on the top 20 in the ranking list determined by the pre-screening tools were weighed in a 1:1 stoichiometric ratio in 15 mL stainless steel SmartSnap™ jars containing two 7 mm stainless steel grinding balls (Form-Tech Scientific, Montreal, Canada). In a LAG experiment, 40 µL of solvent (i.e., ACE, EtAC, EtOH or MeOH) was added. Materials were ground in a Retsch mixer mill MM 400 (Retsch, Germany) for 30 min at a rate of 25 Hz at room temperature. Samples were left to stabilise for 30 min before characterisation by PXRD.

ART with ACA in a 1:1 stoichiometric ratio was also subjected to NG and LAG for 60 min. In addition, ART with ACA in a 2:1 stoichiometric ratio was subjected to LAG with MeOH for 60 min.

Preparation of cocrystal powders and single cocrystal

Cocrystals were prepared by solvent evaporation. Either 1:1 or 2:1 equimolar mixture of ART and ACA was dissolved in a cosolvent of CF and MeOH (90%:10%). The solution was stirred until all solids dissolved at room temperature before being left in a fume cabinet for evaporation. The formation of cocrystals was confirmed by PXRD, FTIR, DSC and HSM. Single cocrystals were also prepared using the same method, but seeded with ART[2]-ACA cocrystal powder obtained. After 3 days the single cocrystals were harvested by natural filtration and then characterised by single crystal XRD, FTIR, and HSM.

Solubility Studies

Apparent equilibrium solubility of ART

Apparent equilibrium solubility of ART was measured by adding excess amount of crystalline materials to a small vial with 20 mL of DDW, which was kept at 37 ± 0.5 °C in a shaking water bath at 150 rpm for 24 h. The supernatant was separated from the suspension by a micro centaur MSB 010.CX2.5 centrifuge (MSE Ltd., London, UK) at 1.3 × 10,000 rpm for 1 min. The supernatant was then diluted to determine the concentration of ART by HPLC. The solid residuals retrieved from tests were analysed by PXRD. All tests were repeated in triplicate.

Cocrystal solubility

The cocrystal solubility was determined by measuring the eutectic point of ART[2]-ACA cocrystals[25, 26]. A series of ACA solutions were prepared in DDW at concentrations of 0.51, 0.99, 1.43, 2.06, 2.63, 3.20, 3.67, 4.30 mg/mL. Excess amount of ART was added to a small vial with 20 mL of each of the prepared ACA solutions, which was kept at 37 ± 0.5 °C in a shaking water bath at 150 rpm for 24 h. The supernatant of each suspension was separated by centrifuge whilst all solid residues were separated by filtration. The concentrations of ART and ACA in the supernatant were analysed by HPLC and UV, respectively. The solid residues were dried naturally and then analysed by PXRD. The eutectic point of the cocrystals was determined by the lowest ACA concentration solution where two solid phases of ART and cocrystal coexisted in equilibrium with the solution[26]. All experiments above were repeated in triplicate.

For a m:n cocrystal of AB without considering the ionisation of each component, its molar solubility is calculated as[6, 27],

$$S_{AB} = \sqrt[m+n]{K_{sp}} = \sqrt[m+n]{A_{eu}^{m} B_{eu}^{n}} \quad (1)$$

where K_{sp} is the solubility product of the A_mB_n cocrystal and concentrations of A_{eu} and B_{eu} are transient molar concentrations of drug and coformer where the solution is in equilibrium with solid drug and cocrystal.

The ratio R_{CO} of a cocrystal solubility via its parent drug A is calculated by,

$$R_{CO} = \frac{S_{AB}}{S_A} \quad (2)$$

where S_A is the molar solubility of the parent drug A.

Powder dissolution studies

Powder dissolution experiments of the parent drug of ART and its cocrystals of ART[2]-ACA were performed under non-sink conditions in DDW. All materials were slightly ground by a mortar and pestle and sieved by a 60-mesh sieve (below 250 µm) to reduce the effect of particle size on the dissolution rates. Each of dissolution tests was carried out via USP Apparatus 2 (paddle) at a speed of 50 rpm in 400 mL of dissolution medium at 37 ± 0.5°C using a PTWS 120D dissolution bath fitted with a variable speed stirrer and heater (Pharma Test). Cocrystals with an equivalent amount of 150 mg of ART were used for non-sink condition tests. Samples of 1 ± 0.1 mL were withdrawn from the dissolution vessel at predefined time points of 5, 10, 15, 30, 60, 120, 180 and 240 min. Supernatants were separated from the samples and analysed by HPLC and UV to determine the concentrations of ART and ACA, respectively. Solid residues retrieved from the non-sink condition experiments were dried at room temperature and analysed by PXRD. All experiments were repeated in triplicate. Dissolution performance parameter (DPP) was used to evaluate the improved dissolution performance of ART[2]-ACA powders in comparison with the parent drug of ART as [26],

$$DPP = \frac{AUC_{ART^2-ACA} - AUC_{ART}}{ART_{ART}} \times 100\% \quad (3)$$

where AUC_{ART^2-ACA} and AUC_{ART} are the areas under the curve (AUC) of dissolution profiles of ART[2]-ACA and ART, indicating the amount of drug dissolved over the period of the dissolution time.

Cocrystal Characterisation

Powder X-ray Diffraction analysis (PXRD)

Powder X-ray diffraction patterns of solids were recorded from range of 2 - 40° (2θ) at a scanning rate of 0.4° (2θ) min^{-1} by a D2 PHASER diffractometer equipped with LYNXEYE XE-T detector (Bruker UK Limited, Coventry, UK). Cu-Kα radiation was used with a voltage of 30 kV and a current of 10 mA.

PXRD and morphology prediction of ART[2]-ACA cocrystals

The simulated PXRD pattern of ART[2]-ACA cocrystals from the single crystal structure was performed using the powder pattern tool in Mercury [Cambridge Crystallographic Data Centre (CCDC), v2020.2.0]. Analysis range of degrees 2θ was set from 2 - 40° with a scanning step size of 0.02° (2θ) at a wavelength of 1.54056 Å. The pattern was set to include hydrogens. The prediction of the morphologies of single crystals was achieved with the Bravais-Friedel-Donnay-Harker (BFDH) crystal morphology tools using the same software.

Single crystal X-ray Diffraction analysis (SXRD)

Suitable single crystals were selected and data collected using a Bruker APEXII CCD diffractometer with Mo Ka radiation (λ = 0.7107 Å). The temperature of the sample was held at 150 K during data collection with an Oxford Cryosystems cryostream. Using Olex2 [28], the structure was solved with the ShelXT[29] structure solution program using Intrinsic Phasing and refined with the ShelXL[30]

refinement package using Least Squares minimisation. Full crystallographic details are given in Table S1 in the electronic supporting information. The resulting structures were deposited with the CCDC (deposition numbers: CCDC 2115273).

Fourier Transform Infrared Spectroscopy (FTIR)

FTIR spectra of the solid samples were measured using an ALPHA interferometer (Bruker UK Limited, Coventry, UK) equipped with a horizontal universal attenuated total reflectance (ATR) accessory. For each sample, an average of 30 scans was collected per spectrum with a resolution of 2 cm^{-1} in the spectral region of 400 to 4000 cm^{-1} using the OPUS software at room temperature.

Differential Scanning Calorimetry (DSC)

The melting point of solids was measured by a NETZSCH DSC 214 Polyma (NETZSCH instrument, Wolverhampton, UK) operated under a nitrogen atmosphere. The instrument was calibrated using indium metal. A sample of between 4 - 8 mg was analysed in an aluminium pan with a pierced pinhole lid. Measurements were carried out at a heating rate of 20°C/min with a temperature range 40 to 200°C.

Hot Stage Microscopy (HSM)

A Mettler Toledo FP82HT hot stage and FP90 controller (Mettler Toledo, Ohio, United States) was used to monitor the thermal events of the cocrystals during heating. The hot stage was connected to a Leica DM750 microscope (Leica Microsystems Ltd, Milton Keynes, UK). The sample was prepared on a slide to cover the pinhole of the hot stage. A heating rate of 20 °C/min in a range of 40 - 200 °C was employed for samples. The video of melting was captured on Studio Capture software.

High-Performance Liquid Chromatography (HPLC)

Concentrations of ART in solution were determined by a PerkinElmer series 200 HPLC (PerkinElmer Ltd, Beaconsfield, UK) with a Restek C18 column (5 µm, 150 × 4.6 mm) (Restek Thames, High Wycombe, UK) at 20 °C. An isocratic method was used with 40% double distilled water and methanol (mixed in a 3:2 ratio) and 60% acetonitrile at 0.5 mL/min flow rate and a wavelength of 206 nm for detecting ART concentration was used. The calibration model is shown in Table S6 in the supporting materials.

Ultraviolet-Visible spectroscopy (UV)

Concentrations of ACA in solution were determined by a Thermo Spectronic Helios Gamma 9423 1702E UV Spectrophotometer (Fisher Scientific, Loughborough, UK) at room temperature. The UV spectrometer was blanked using DDW and samples were analysed at wavelength of 260 nm, at which ART has no overlapping shown in Fig. S2. The calibration model and validation by the mixture of ART and ACA are shown in Tables S6 and S7 respectively in the supporting material.

Results and Discussion

Ab intro Screening

Forty-eight structures were retrieved based on the CSD search using the keywords of artemisinin and its molecular structure detailed in Table S2 in the supporting materials. There are two polymorphs of ART, with space groups of $P2_1\,2_1\,2_1$ (CSD references: JAQTED, QNGHSU, QNGHSU02, QNGHSU03, QNGHSU10, QNGHSU11) and P1 (CSD reference: QNGHSU01)[12]. There are two ART cocrystals deposited, i.e., 1:1 artemisinin and orcinol (CSD reference: TALCUG) and 2:1 artemisinin and resorcinol (CSD reference: TALCOA)[13]. Thirty-seven structures correspond with solvates or derivates of Artemisinin. Interestingly amongst them, seven structures corresponded to ART derivative of 11-aza-artemisinin cocrystals with maleic acid (1:1 and 2:1), fumaric acid (2:1), trans-cinnamic acid, pimelic acid (2:1), 4-bromosalicylic acid and 5-bromosalicylic acid[31, 32].

A survey of the CSD (v2020) was performed to identify probable coformers for ART cocrystal development. The 75 coformers that were tested in the previous publication was not included[13]. A total of 80 potential coformers were chosen from the CSD including a list of common drugs and nutraceuticals. Based on the molecular complementarity prediction by the CSD screening tool, it was found that 39 out of 80 passed the initial screening shown in Table S3.

The probability of cocrystal formation between ART and a coformer selected was also calculated using the virtual cocrystal screening tools[20]. After geometry optimisation, the MEPSs of ART and 80 coformers were generated using Spartan18 (v1.4.5). Potential hydrogen bonding sites of ART with coformers are the maximal positive potential region at the hydrogen of methyl group located at C9 and the minimal negative potential region at oxygen (O2) located at C12 on ART's MEPS (Fig 2a). The difference between the interaction site pairing energies of the potential 1:1 cocrystal of two pure compounds and its probability of a cocrystal formation are shown in Table S3, where the coformers were ranked in order of highest probability of forming a cocrystal with ART. Top 20 coformers have potential to form cocrystals with ART at the probability of 50% above, therefore, they were chosen for experimental screening. As expected, these coformers all contain strong H-bond donors, and most of the 20 coformers are either carboxylic acids or phenols, detailed can be found in MEPSs shown in Table S4 in the supporting materials.

It is worth noting that there is a significant discrepancy between the two computational screening methods. Among the top 20 coformers predicted by the virtual cocrystal screening tool, only 8 coformers show "passed" by the molecular complementarity prediction tools. ACA is of a high probability to form a cocrystal with ART at 95.40% and its MEPS [in Fig. 2(b)] shows the H-bond donors and H-bond acceptors at the both ends of the molecule. However, ACA failed the initial screening by the complementarity prediction tool.

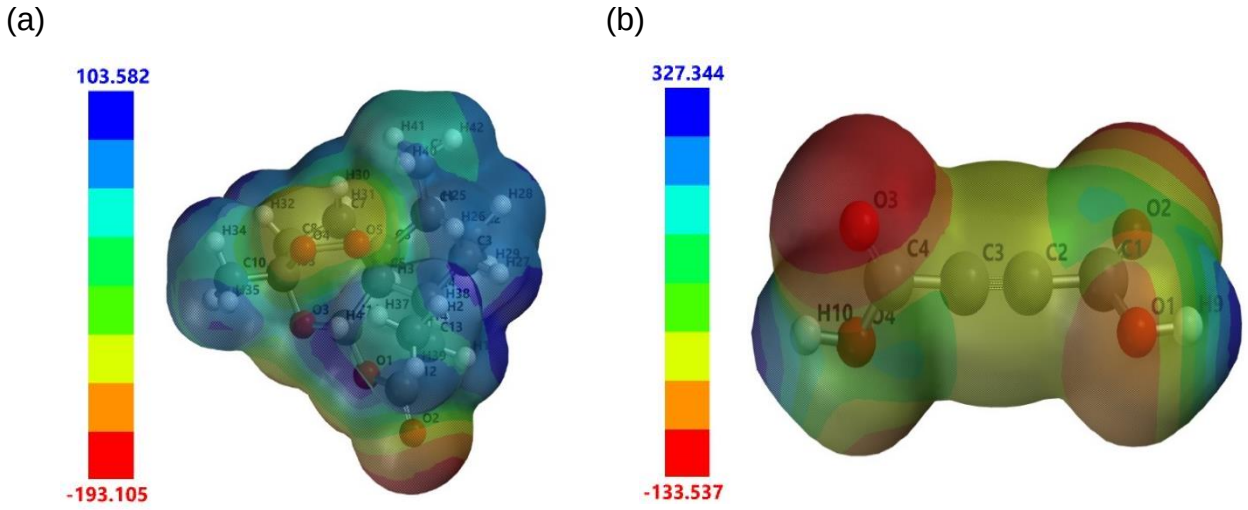

a. Artemisinin b. Acetylenedicarboxylic

Fig. 2: Molecule electrostatic potential surfaces

Experimental screening

Experimental screening experiments were carried out for a 1:1 mixture of artemisinin and each of the selected coformers using both NG and LAG methods. Four different solvents were used in LAG, including ACE, EtAC, EtOH or MeOH. In all cases, the resultant solids were analysed using PXRD. When comparing to the starting materials, the PXRD pattern of a product that exhibits new diffraction peaks and/or the absence of peaks usually indicates the formation of a new crystalline form. In summary, the potential coformers for formation of a new crystalline phase with ART include HBD, HCT, AQD, HEDP and ACA.

ART with HBD did show a new peak in LAG with acetone, however, there is no loss of ART peaks shown in Table S5 in the supporting materials. Further study indicated that the peaks were generated by phase transformation of HBD affected by acetone. Similar phenomena were observed for HCT, AQD and HEDP due to phase transformation induced by a solvent and/or grinding. Table S5 in the supporting materials shows the PXRD patterns for all coformers.

The key characteristic peaks of ART at 2θ [Fig.3(b)] are 7.25°, 11.74°, 14.46°, and 21.87°, which correspond to orthorhombic polymorph[12]. There are three characteristic peaks of ACA are observed at 11.91°, 23.72°, and 27.75° of 2θ shown in Fig. 3(b). For a 1:1 mixture of ART and ACA, a partial transformation into a new solid phase was observed by a 30 min NG and LAG with all solvents (i.e., ACE, EtAC, EtOH or MeOH) shown in Fig. 3 (a), where the new peak at 11.00° appeared for the resultant grinding product. However, the ART characterisation peak at 11.74° still presented in the product. Varying the grinding time from 30 to 60 mins, a complete transformation of cocrystals were observed for LAG with MeOH where loss of ART and ACA characterisation peaks at 11.74° and 11.91° respectively and gain of new peaks at 11.00° and 13.92°, shown in Fig. 3(b).

When the single cocrystal structure was determined from SXRD, surprisingly it was a 2:1 ART-ACA cocrystal. Further investigations were conducted for the results of grinding of 2:1 mixture of ART and ACA, indicating that they were mixtures of ART and ART^2-ACA cocrystals, where the new peaks at 11.00° and 13.92° appeared and ART characterisation peak at 11.74° did not disappear in Fig. 3(b). This phenomenon was observed in formation of 2:1 meloxicam and ACA cocrystals because some of ACA converted to its monohydrate or amorphous form on grinding, not participating cocrystallisation[24]. Therefore, ART^2-ACA cocrystals were formed from 1:1 mixture of ART and ACA.

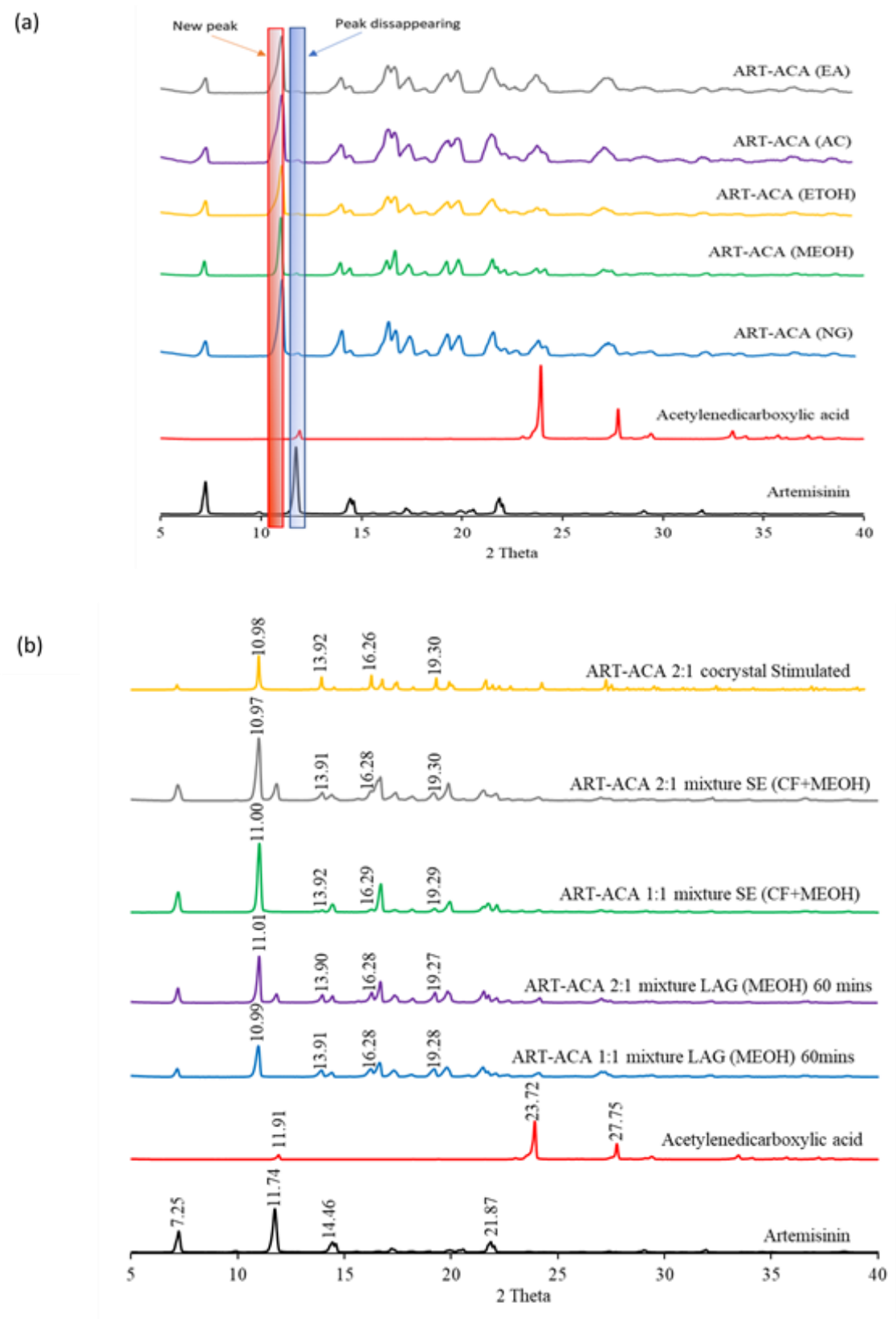

Fig. 3: PXRD patterns for experimental screening: (a) 1:1 mixture of ART and ACA for 30 minutes; (b) LAG of 1:1 and 2:1 mixture of ART and ACA for 60 minutes with MEOH, solvent evaporation (SE) in cosolvent of CF and MEOH and cocrystal simulation

ART²-ACA characterisation and structure analysis

ART²-ACA cocrystal powders from 1:1 or 2:1 mixture of ART and ACA were prepared by solvent evaporation using a mixture of chloroform (CF, 90%) and methanol (MEOH,10%). Pure ART²-ACA powders can only be obtained from 1:1 mixture of ART and ACA by solvent evaporation while as mixtures of ART and ART²-ACA cocrystals were obtained from 2:1 mixture of ART and ACA, shown in Fig. 3(b), which is consistent with those obtained by LAG in the presence of MEOH.

The thermal behaviour of ART²-ACA powders synthesised were investigated using HSM in Fig. 4, which was compared with the individual components of ART and ACA. It is shown that ART²-ACA crystals melt at 119.3°C, which is significantly lower than the melting point of ART at 153.3°C or ACA at 185.3°C. Although the melting temperatures of most of cocrystals are between the values of individual components, a considerable number of cocrystals (ca. 31%) with the melting temperatures are lower than those of individual components[33]. A lower melting point of ART²-ACA powders could indicate improved solubility of ART due to less energy required to break down the crystal lattice energy for dissolution. In contrast, the DSC results of ART²-ACA cocrystals and individual components are showed in Fig. S1 in the supporting materials, indicating that ART²-ACA cocrystals obtained were contaminated by amorphous ACA. The exothermic peak was caused by recrystallisation of amorphous form of ACA. Currently research work is undertaken to explore the issue.

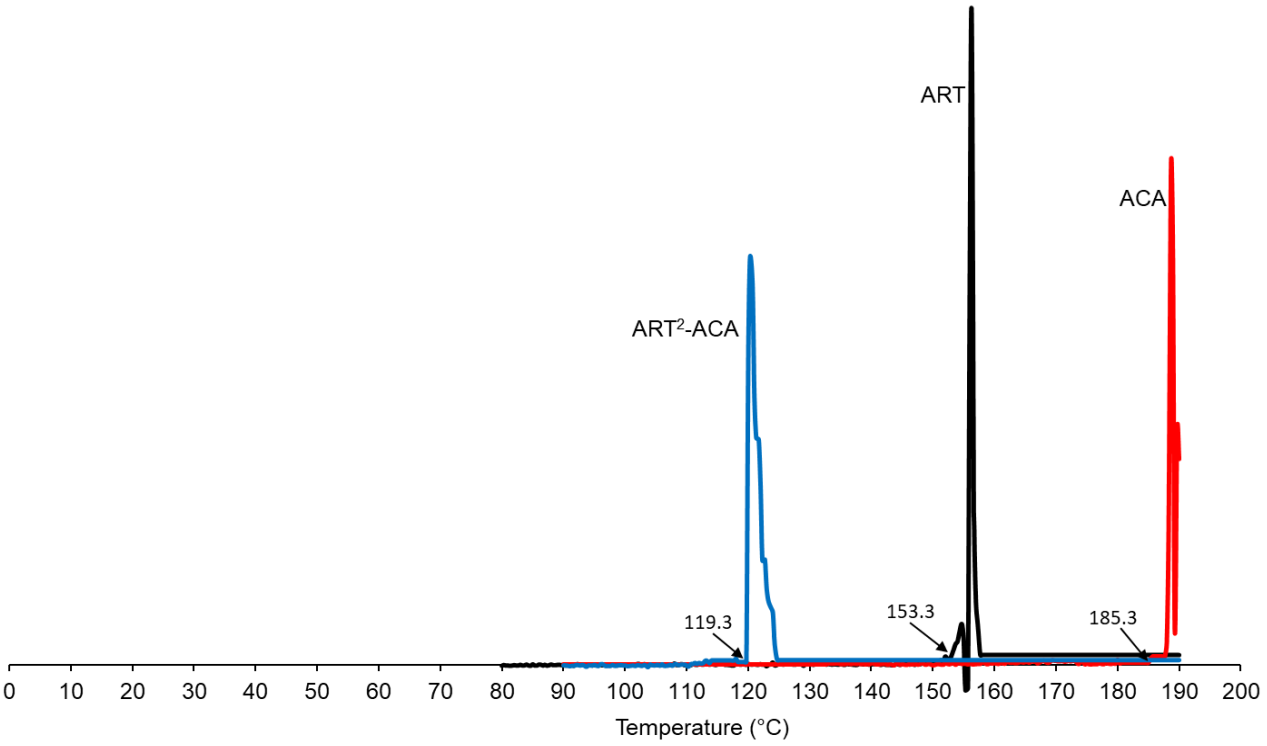

Fig. 4: Comparion of HSM thermographs of ART, ACA and ART²-ACA

Infrared spectroscopy can be used to identify the formation of cocrystals because the measured spectrum is sensitive to changes in intermolecular interactions of the solid compounds. The cocrystal infrared spectrum should exhibit different vibrational frequencies compared with those of the parent API and coformer. As shown in Fig. 5, the assignment of key ART characteristic peaks are as follows: 1025 cm^{-1} and 1011 cm^{-1} attributed to -C-O- stretching vibrations, 1113 cm^{-1} contributed to -O- stretching vibrations, 1733 cm^{-1} contributed to C=O stretching vibrations, 2975 cm^{-1} and 2951 cm^{-1} contributed to -CH2 stretching vibrations[34]. ACA contains two O-H and C=O whose characteristic peaks are observed at 2958 cm^{-1} and 1677 cm^{-1} respectively and the peak at 2509 cm^{-1} is contributed to C≡C stretching [35]. ART characteristic

peaks at 2975, 2951 and 1733 cm^{-1} have shifted to 2978, 2954 and 1721 cm^{-1} and ACA characteristic peaks at 1677 cm^{-1} have shifted to 1689 cm^{-1} for ART^2-ACA.

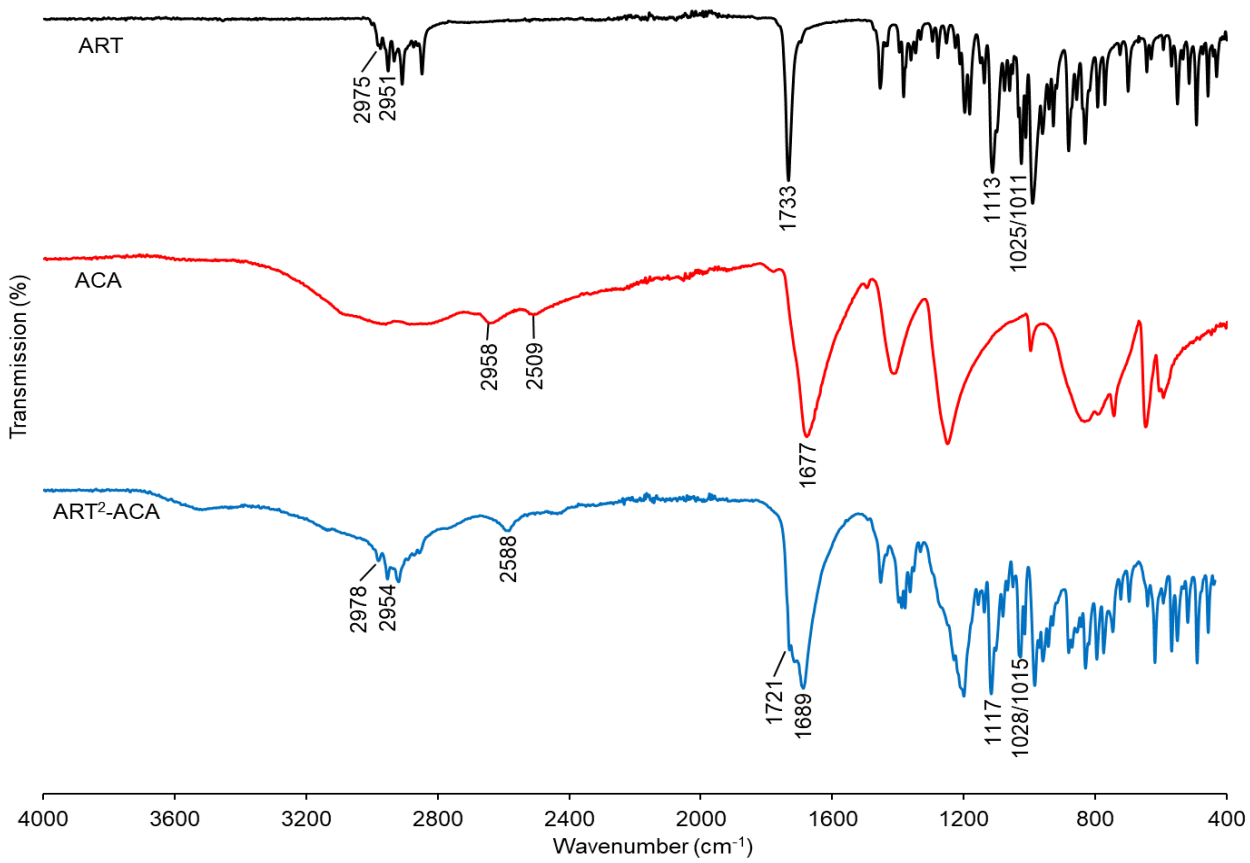

Fig. 5: Comparison of FTIR spectra of ART, ACA and ART^2-ACA

High-quality single crystals of ART^2-ACA for XRD measurements were obtained through slow seeded evaporation in a mixture of CF (90%) and MEOH (10%) using a stoichiometric ratio of ART- ACA (1:1). ART^2-ACA crystallises as orthorhombic crystals [Fig. 6(a)]. The crystal structure of ART^2-ACA was determined by SXRD to confirm cocrystal formation. ART^2-ACA crystallises in an orthorhombic unit cell with the space group P $2_12_12_1$ and cell parameters a = 10.5089 Å, b = 24.083 Å, c = 6.4952 Å. The asymmetric unit of cocrystal contains one ART molecule and a half molecule of ACA held together by O(1A)•••H-O(2B) and O(1A)•••H-O(2B_a) intermolecular interactions [Fig. 6(b)]. These trimers are linked through weaker CH…O hydrogen bonds to form a 1-D molecular ribbon structure along the a-axis of the crystal [Fig. 6(c)]. ACA molecule, assembled into discrete trimeric units held together by O(1A)•••H-O(2B) and O(1A)•••H-O(2B_a) intermolecular interactions (Fig 6(b). These ribbons are then stacked along the c-axis of the crystal by further CH…O interactions before the final 3-D structure is constructed through CH…O interactions linking the columns together [Fig. 6(d)]. The morphology of the cocrystals was predicted, based on the crystallographic data, using the Bravais-Friedel-Donnay-Harker (BFDH) morphology tool from the Mercury software (CCDC v2020.2.0) [Fig. 6(e)], which matched well with the experimental single crystal [Fig. 6(a)]. Meanwhile, based on the crystallographic data, the PXRD pattern of ART^2-ACA can also be simulated [Fig. 3(b)], which matched well with the measured characteristic peaks at 11.00° and 13.92° of 2θ.

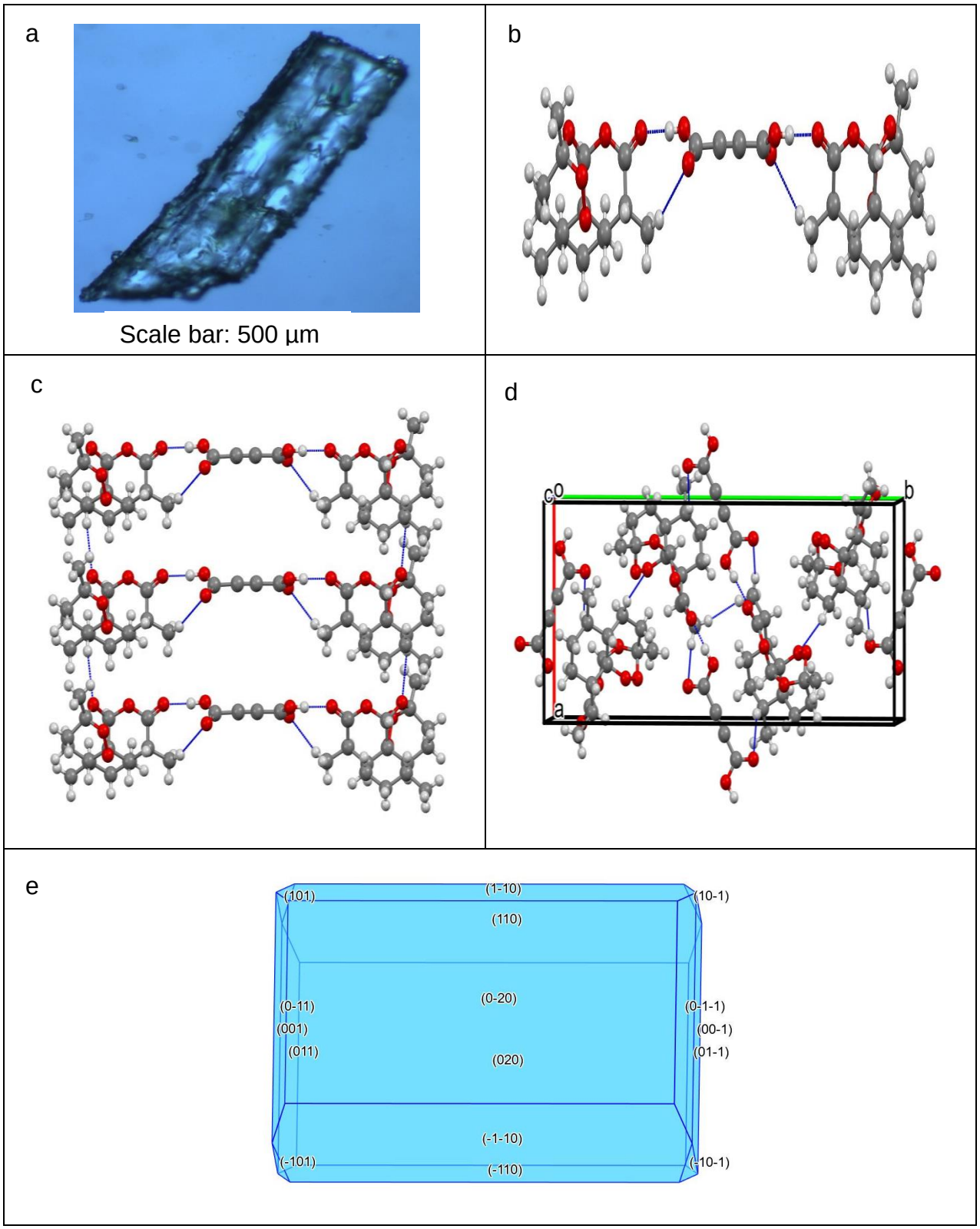

Fig. 6: The structure and packing ART[2]-ACA: a) Single crystal under polarised light microscope; b) supramolecular synthon linked trimer; c) 1D network; d) unit cell (viewed along the c-axis); e) predicted morphology.

Solubility and dissolution studies

The solubility and dissolution rate of ART[2]-ACA cocrystals and its parent drug of ART were examined. The equilibrium solubility of ART was 90.1±0.6 µg/ml (0.319 mM) in DDW at 37°C. The apparent solubility of ART was measured in the presence of ACA [Fig. 7(a)] in DDW at 37°C, which was used to determine the solubility of ART[2]-ACA cocrystals. The concentrations of ART and ACA were determined after equilibration for 24 h when excess amount of ART was added into each of the prepared ACA solutions shown in Fig. 7(a). The solubility of ART initially increased with increasing the ACA concentration due to soluble complex formation between the two compounds. When the ACA concentration exceeded 2.63 mg/mL, the apparent solubility of ART increased slightly, indicating that the solubility limit of the complex formed was exceeded and the concentration of ART in solution did not change significantly, where 16% increase in the apparent solubility of ART was observed in comparison to ART solubility in DDW alone.

At an ACA concentration of 1.43 mg/mL and above, the precipitation of ART[2]-ACA started and two phases, i.e., ART and ART[2]-ACA, could be observed for the solid residues in the solution [Fig. 7 (b)]. The concentrations measured for ART and ACA in the 1.43 mg/mL ACA solution represented the transition concentration of ART[2]-ACA[20], i.e., 0.357 mM for ART and 11.327 mM for ACA. So, according to the definition of cocrystal solubility in Eq. (1), the solubility of ART[2]-ACA was 2.024 mM, which was 6.34-fold higher than the solubility of ART calculated by Eq. (2).

The dissolution profiles of ART and ART[2]-ACA are illustrated in Fig. 8. The dissolution of ART was slower and after 4 h, its concentration was 71.95 µg/mL. In contrast, the dissolution rate of ART[2]-ACA was faster, the concentration of ART reached was 83.76 µg/mL. In terms of the dissolution performance parameter (DPP), ART[2]-ACA showed a 16% increase in comparison to ART. It was also worth noting that the solids residues, following dissolution of ART[2]-ACA, were ART, as confirmed by PXRD (Fig. S3 in the supporting materials), suggesting an occurrence of phase transformation during the dissolution of ART[2]-ACA.

(a)

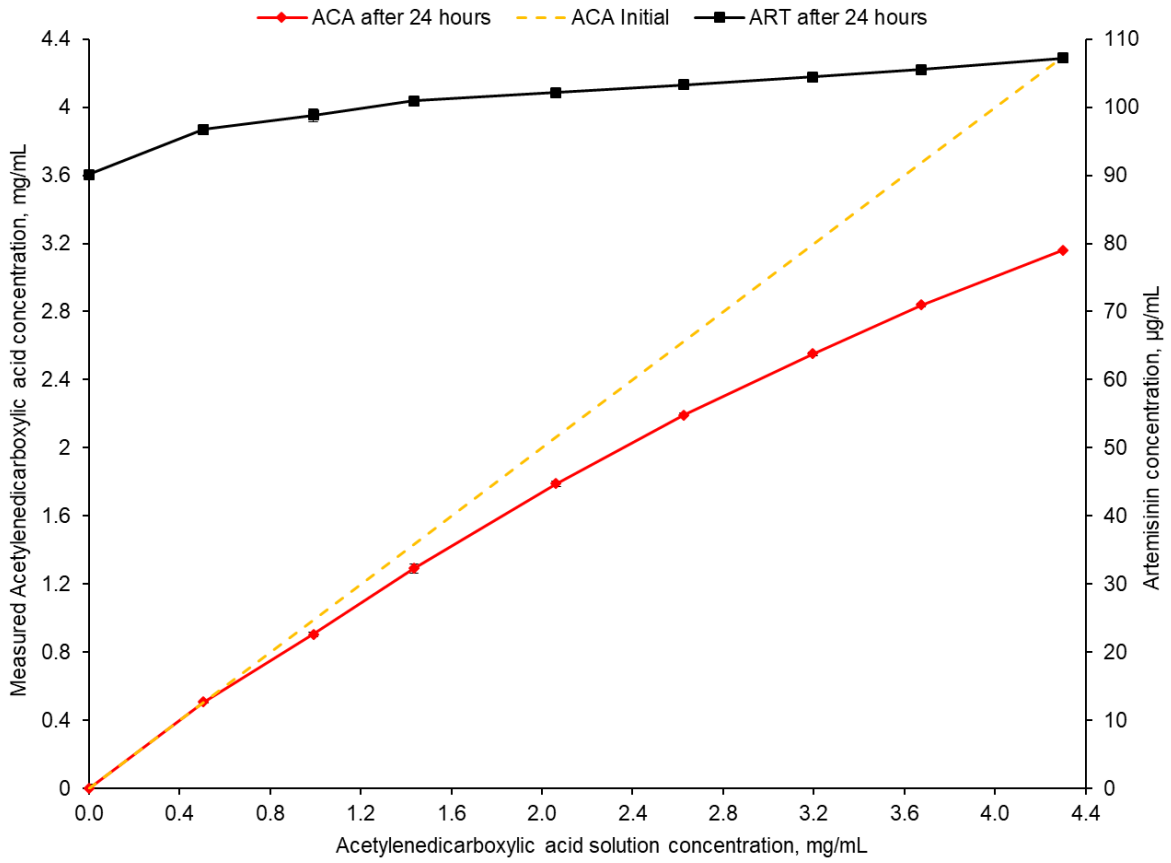

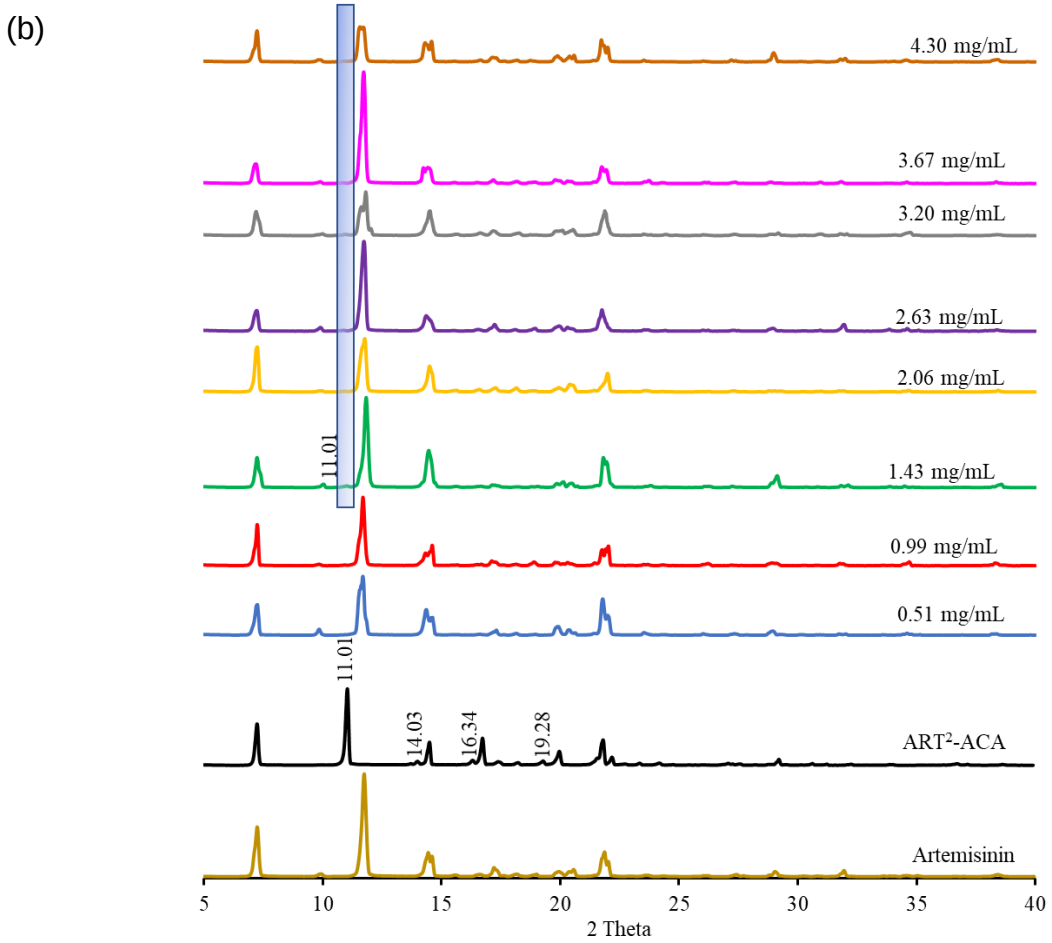

Fig. 7: Apparent solubility of ART in the presence of ACA at different concentrations. (a) The concentrations of ART and ACA at equilibrium; (b) PXRD observations of the solid residues.

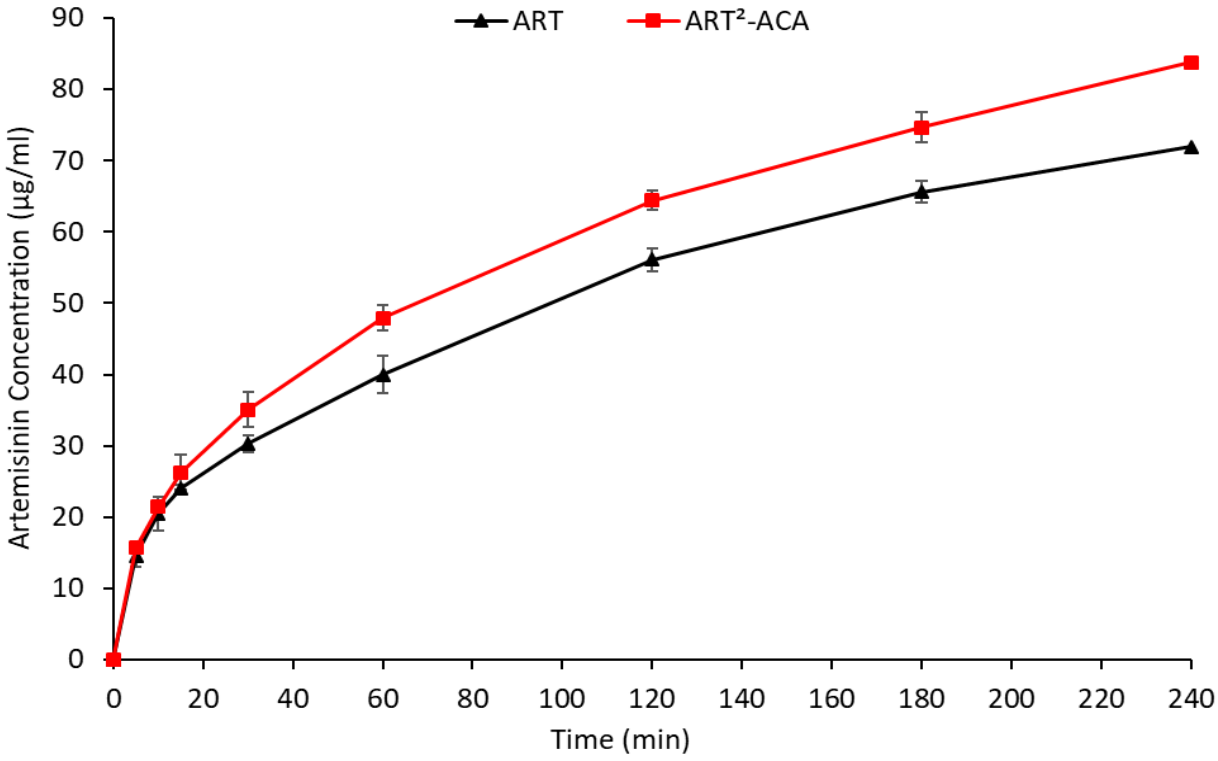

Fig. 8: Powder dissolution profiles of ART and ART^2-ACA under non-sink conditions

Conclusions

Artemisinin is used to treat multi-drug resistant strains of malaria and is also in the early stages of development as an anti-cancer drug. The limitation of ART's solubility and bioavailability can be improved by solubility enhancement methods such as a cocrystallisation approach. Computational screening provided an initial prediction for the successful preparation of novel cocrystal of artemisinin and acetylenedicarboxylic acid via grinding and solution methods. ART^2-ACA cocrystals belong to the *P* $2_12_12_1$ space group of the orthorhombic system formed O(1A)•••H-O(2B) and O(1A)•••H-O(2B_a) intermolecular interactions between ART and ACA. ART^2-ACA showed increased solubility and dissolution performance in comparison to ART. The solubility of ART^2-ACA was 6.34-fold higher than the solubility of ART. The dissolution rate of ART^2-ACA showed a 16% increase for its dissolution performance parameter in comparison to ART. It is worth noting that initial computational screening could be problematic and contradictive, depending on the tools used. Therefore, experimental screening is always needed to discover novel cocrystals. To the best of our knowledge, this is the first ART cocrystal with a carboxylic acid which may aid the future discovery of more ART cocrystals with carboxylic acids in the future for pharmaceutical applications.

Author Contributions

J.M. conducted the experiments, prepared and analysed the samples, performed the data analysis, and prepared the manuscript. S.J.M. conducted the dissolution and solubility experiments. R.A. provided guidance and reviewed the manuscript. C.C.S conducted single cocrystal structure measurement and analysis and reviewed the manuscript. M.L. conceptualized the project and acquired funding for the whole study, directed the study, determined the experimental methods, completed the pre-experiment, analysed and discussed the results, and prepared the manuscript.

Conflicts of interest

There are no conflicts to declare

Acknowledgements

We would like to thank the financial support of the work by UK Engineering and Physical Sciences Research Council (EPSRC, EP/R021198/1).

Notes and references

1. J. Benjamin, B. Moore, S. T. Lee, M. Senn, S. Griffin, D. Lautu, S. Salman, P. Siba, I. Mueller and T. M. Davis, *Antimicrobial agents and chemotherapy*, 2012, **56**, 2465-2471.
2. D. Chaturvedi, A. Goswami, P. P. Saikia, N. C. Barua and P. G. Rao, *Chemical Society Reviews*, 2010, **39**, 435-454.
3. G. A. Balint, *Pharmacology & therapeutics*, 2001, **90**, 261-265.
4. J. Wong and K. Yuen, *International Journal of Pharmaceutics*, 2001, **227**, 177-185.
5. W. E. Ho, H. Y. Peh, T. K. Chan and W. F. Wong, *Pharmacology & therapeutics*, 2014, **142**, 126-139.
6. M. Kaur, V. Yardley, K. Wang, J. Masania, A. Botana, R. R. Arroo and M. Li, *Molecular Pharmaceutics*, 2021, **18**, 4256-4271.
7. N. Ibrahim, H. Ibrahim, A. M. Sabater, D. Mazier, A. Valentin and F. Nepveu, *International journal of pharmaceutics*, 2015, **495**, 671-679.
8. C. Woodrow, R. Haynes and S. Krishna, *Postgraduate medical journal*, 2005, **81**, 71-78.

9. N. Qiao, M. Li, W. Schlindwein, N. Malek, A. Davies and G. Trappitt, *International journal of pharmaceutics*, 2011, **419**, 1-11.
10. N. Shan, M. L. Perry, D. R. Weyna and M. J. Zaworotko, *Expert opinion on drug metabolism & toxicology*, 2014, **10**, 1255-1271.
11. N. J. Babu and A. Nangia, *Crystal Growth & Design*, 2011, **11**, 2662-2679.
12. E. Horosanskaia, A. Seidel-Morgenstern and H. Lorenz, *Thermochimica Acta*, 2014, **578**, 74-81.
13. K.-L. Chan, K.-H. Yuen, H. Takayanagi, S. Janadasa and K.-K. Peh, *Phytochemistry*, 1997, **46**, 1209-1214.
14. S. Karki, T. Friščić, L. Fábián and W. Jones, *CrystEngComm*, 2010, **12**, 4038-4041.
15. M. Kaur, V. Yardley, K. Wang, J. Masania, R. R. Arroo, D. B. Turner and M. Li, *Molecular Pharmaceutics*, 2021, **18**, 4272-4289.
16. B. S. Lynch, E. S. Delzell and D. H. Bechtel, *Regulatory toxicology and pharmacology*, 2002, **36**, 198-210.
17. X. Wang, G. Li, P. Li, L. Huang, J. Huang and H. Zhai, *Pharmaceutical biology*, 2015, **53**, 876-881.
18. A. Delori, P. T. Galek, E. Pidcock and W. Jones, *Chemistry–A European Journal*, 2012, **18**, 6835-6846.
19. P. T. Galek, L. Fabian, W. S. Motherwell, F. H. Allen and N. Feeder, *Acta Crystallographica Section B: Structural Science*, 2007, **63**, 768-782.
20. D. Musumeci, C. A. Hunter, R. Prohens, S. Scuderi and J. F. McCabe, *Chemical Science*, 2011, **2**, 883-890.
21. T. Grecu, H. Adams, C. A. Hunter, J. F. McCabe, A. Portell and R. Prohens, *Crystal growth & design*, 2014, **14**, 1749-1755.
22. T. Grecu, C. A. Hunter, E. J. Gardiner and J. F. McCabe, *Crystal growth & design*, 2014, **14**, 165-171.
23. A. Delori, I. B. Hutchison, C. L. Bull, N. P. Funnell, A. J. Urquhart and I. D. Oswald, *Crystal Growth & Design*, 2018, **18**, 1425-1431.
24. C. Tantardini, S. G. Arkhipov, K. A. Cherkashina, A. S. Kil'Met'Ev and E. V. Boldyreva, *Acta Crystallographica Section E: Crystallographic Communications*, 2016, **72**, 1856-1859.
25. L. Bolus, K. Wang, C. Pask, X. Lai and M. Li, *Journal of Molecular Structure*, 2020, **1222**, 128893.
26. M. Guo, K. Wang, N. Qiao, L. Fábián, G. Sadiq and M. Li, *Molecular pharmaceutics*, 2017, **14**, 4583-4596.
27. D. J. Good and N. Rodriguez-Hornedo, *Crystal Growth and Design*, 2009, **9**, 2252-2264.
28. A. OLEX, *J. Appl. Crystallogr*, 2009, **42**, 339-341.
29. G. M. Sheldrick, *Acta Crystallographica Section A: Foundations and Advances*, 2015, **71**, 3-8.
30. G. M. Sheldrick, *Acta Crystallographica Section C: Structural Chemistry*, 2015, **71**, 3-8.
31. M. Roy, K. Li, M. Nisar, L.-Y. Wong, H.-Y. Sung, R. K. Haynes and I. D. Williams, *Acta Crystallographica Section C: Structural Chemistry*, 2021, **77,** 262-270.
32. M. Nisar, H. H.-Y. Sung, H. Puschmann, R. Lakerveld, R. K. Haynes and I. D. Williams, *CrystEngComm*, 2018, **20**, 1205-1219.
33. G. L. Perlovich, *CrystEngComm*, 2015, **17**, 7019-7028.
34. H. Yu, X. Zhao, Y. Zu, X. Zhang, B. Zu and X. Zhang, *International journal of molecular sciences*, 2012, **13**, 5060-5073.
35. M. Zidan, A. Allaf, A. Allahham and A. Al-Zier, *Optics & Laser Technology*, 2015, **68**, 60-66.